AIAA 2003-5055

Simulation of the Cold-Wall Swirl Driven Combustion Chamber

D. Fang and J. Majdalani
Marquette University
Milwaukee, WI 53233

M. J. Chiaverini
Space Center
Orbital Technologies Corporation (ORBITEC)
Madison, WI 53717

39th AIAA/ASME/SAE/ASEE Joint Propulsion Conference and Exhibit
20–23 July 2003
Huntsville, AL

39th AIAA/ASME/SAE/ASEE Joint Propulsion Conference and Exhibit
20-23 July 2003, Huntsville, Alabama

AIAA 2003-5055

Simulation of the Cold-Wall Swirl Driven Combustion Chamber

Dianqi Fang* and Joseph Majdalani†
Marquette University, Milwaukee, WI 53233
and
Martin J. Chiaverini‡
Orbital Technologies Corporation, Madison, WI 53717

This study provides the numerical simulation of an innovative, cold-wall bidirectional vortex combustion chamber (CWBVCC). The vortex flow configuration in this chamber is unique in that the oxidizer is typically injected tangentially into the combustion chamber, and the process results in a swirling combustion field that inherently separates into two distinct coaxial zones: an outer vortex stream circulating towards the head end and an inner concentric vortex spiraling in the opposite direction. The inner swirl increases fuel residence time, turbulence, and propellant mixing, thus improving overall efficiency and thrust. The spinning vortices also provide an extended flow path much longer than the geometric length of the chamber, thus allowing for shorter chamber lengths. The outer vortex protects the chamber walls from excessive heating loads via convective cooling, thus resulting in lower wall temperatures. This feature not only reduces cooling requirements, but also permits more flexibility in material selection that can ensure durability and reduced weight. Through the cold flow simulation, the existence of a bi-directional flow is demonstrated and the spatial invariance of the so-called mantle (that separates inner and outer vortex regions) is confirmed. According to these simulations, the cold wall effect is extrapolated from the temperature maps and species mass fractions distributed over the combustion chamber. Our simulations further indicate that the oxidizer flow entering the chamber does not short circuit toward the nozzle but is rather compelled to spiral toward the head end where fuel is supplied through radial injectors. The need for secondary oxidizer injection at the head end is found to be instrumental under reactive flow conditions.

I. Introduction

THE application of swirl has been extensively used as a vehicle for efficient and stable combustion in industrial furnaces, utility boilers, spiral heat exchangers, gas turbines with toroidal zones, turbofans with swirl augmenters, and internal combustion engines. Unlike columnar flow, cyclonic flows are characterized by a bidirectional coaxial motion that is not caused by vortex breakdown or instability. One of the earliest investigations of cyclonic motions was carried out by ter Linden[1] whose efforts have focused on determining the influence of geometric parameters on the separation efficiency in dust separators. In subsequent years, a simple yet fully analytical model for the flow in a conical cyclone was advanced by Bloor and Ingham.[2] Confirmatory CFD numerical simulations were later carried out by Hsieh and Rajamani,[3] Hoekstra, Derksen and Van den Akker,[4] Derksen and Van den Akker,[5] and others. Hoekstra and co-workers also conducted laboratory tests using laser-doppler velocimetry (LDV) to verify their multi-phase numerical simulations.[4]

The exploitation of CFD software for the numerical approximation of core gas dynamics is becoming more and more the generic method of choice. In principle, it stands to yield efficacious predictions regarding the collective performance of a cyclonic burner or a swirl-based thrust chamber. In the field of confined swirling flow, an important issue that is not yet fully understood is the viability of a given turbulence closure model. Many questions remain un-answered as far as the bidirectional vortex flow is concerned. For example, issues regarding vortex precessing, instability and breakdown remain to be assessed for different chamber aspect ratios and inlet/outlet flow conditions. The identification of a turbulence model that is sufficiently flexible to capture the core flow interactions in a turbulent swirling field is clearly crucial for the success of future CFD explorations. The search for a portable turbulence model is also needed to permit investigations of compressible and incompressible flow ranging from low to high speed under both cold flow and reactive conditions.

Three-dimensional simulations in a complexly shaped flow domain can be computationally very

demanding, especially using the advanced turbulence models that are described in the literature. These will be necessary to capture the anisotropy of the turbulence field induced by swirl. Many articles dealing with single-phase flow predictions in cyclones treat the flowfield as being axisymmetric and steady.[6-8] Some of the earliest results on modeling gas cyclone separators by use of CFD were actually obtained by Boysan, Ayers and Swithenbank.[6] These have applied the algebra stress model (ASM) to compute the six components Reynolds stress. More recent work on the modeling of cyclonic flow employed the standard $\kappa-\varepsilon$ model, modified $\kappa-\varepsilon$ model, and the Renormalization-group, RNG-$\kappa-\varepsilon$ model.

According to Hoekstra, Derksen and Van den Akker,[4] a more successful, but computationally more expensive turbulence model is the Reynolds Stress Transport Model (RSTM, aka RSM). When using this scheme, the transport of each Reynolds stress is described by its own partial differential equation. Hoekstra and co-workers found that both the $\kappa-\varepsilon$ model and the RNG-$\kappa-\varepsilon$ model predicted an unrealistic distribution of axial and tangential velocities and, hence, were deemed unsuitable for cyclonic flow analysis. Results obtained using the Reynolds stress transport model were in reasonable agreement with the experimental data, although some discrepancies existed that pled for further refinement.

At present, there seems to be a number of intriguing issues that motivate a three-dimensional and time-resolved simulation of the bi-directional vortex. Because cyclones exhibit a highly nonaxisymmetric, low-frequency instability (i.e., the processing vortex core known as PVC), the 3-D structures exhibited by the asymmetric excursions of the vortex tube can only be captured with a 3D study. In the past, a 3-D average flowfield predicted with a high level of accuracy was achieved by Derksen and Van den Akker[9] using a standard Smagorinsky sub grid-scale model (LES). The sub grid-scale model seemed to be a favorable approach to turbulence modeling of an intrinsically unsteady flow. As opposed to turbulence models based on the Reynolds Navier-Strokes (RANS) equations, LES has the capability of distinguishing between the scales that are resolved and the scales that are modeled. The question regarding which model will be optimal for the chemically reactive simulation with single and/or multi-component, multi-phase flow remains to be answered.

Unlike cyclonic flows that possess dual outlets, the bidirectional coaxial field observed in the liquid propellant thrust chamber has only one outlet section. It is believed that the 3-D simulation will illustrate the influence of geometric and fluid flow design parameters on the morphology of the flowfield and its influence on propellant combustion processes and engine performance.

II. Computational Model

The first step in carrying out the CFD simulation is to set up the geometric mesh. We use a commercial software (Gambit 2.0 by Fluent[10]) to create the geometry and the required mesh. The chamber's geometric details are provided in Fig. 1 and Table 1. The combination of 2-in ID, 2-in chamber length, and 0.5-in throat provide an approximate L* of 32 in. The chamber also has a contraction ratio of 16 and a nozzle area ratio of 2. The contraction ratio CR is the chamber cross section divided by the throat area.

The main GOX injector is a 4-port swirl injector located just forward of the nozzle plate. A secondary GOX injector (1-port radial injector) is oriented along the chamber axis to facilitate core burning. The GH2 injector is located just below the faceplate and has 4 radial ports (see Table 1 and Fig. 1).

In order to maintain the number of cells as low as possible it was first decided that the hexahedral and quadrilateral cells were to be used whenever possible. Otherwise, the tetrahedral cells are defaulted to. However, a problem was encountered. The angle between the sidewall and the tangential injectors at their intersection points was nearly 180 degrees; this caused the elements of that portion of the domain to be highly skewed, thus reducing the mesh quality. To avoid this problem, the volume was decomposed into several volumes that were meshed separately. After several trials, the mesh was developed by implementing throughout the entire domain a tet/hybrid scheme while keeping the interval count at 50. The increased mesh density near the wall of the combustion chamber was intended to enable the resolution of rapid changes within the boundary layer. Then, along inlets and outlets, inflow and outflow boundary conditions were imposed.

Having generated the geometric grid and defined its boundary types, the resulting mesh file was imported into a commercial solver running on a P4 computer at 2.53GHz under Windows XP with 3GB of RAM. The simulation was based on a steady, 3-D, segregated, implicit solver.

Next, a turbulent scheme was chosen to model the viscous incompressible flow. In Fluent™, there are two alternative methods: i) Reynolds averaging and ii) filtering. The first is employed to transform the Navier-Stokes equations in such a way that the small-scale turbulent fluctuations do not have to be directly simulated. The Reynolds-averaged Navier-Stokes (RANS) equations represent transport equations for the mean flow quantities only, with all the scales of the turbulence being modeled. It is generally adopted for practical engineering calculations, and uses models such as Spalart-Allmaras, $\kappa-\varepsilon$ and its variants, $\kappa-\omega$ and its variants, and the RSM.

Filtering, on the other hand, is essentially a manipulation of the exact Navier-Stokes equations to remove only the eddies that are smaller than the size of the filter (which is usually taken as the mesh size). In LES, the large eddies are computed in a time-dependent simulation that uses a set of "filtered" equations. By modeling less and solving more, the error induced by the turbulence model is considerably reduced. However, the application of LES to industrial fluid simulations is still in its infancy. As highlighted in a recent review publication, typical applications to date have been for simple geometries. This is mainly because of the large computer resources required to resolve the energy-containing turbulent eddies. For these many reasons, the LES model was abandoned.

As for the Reynolds averaging approach, the Boussinesq hypothesis which is often employed to relate the Reynolds stresses to the mean velocity gradients is used in the Spalart-Allmaras model, the $\kappa-\varepsilon$ models, and the $\kappa-\omega$ models. The Reynolds Stress Transport Model is the most elaborated turbulent model that our commercial software provides and the one that accounts for the effects of streamline curvature, swirl, and rapid changes in strain rate in a more rigorous fashion than one-equation and two-equation models; it has greater potential to yield accurate predictions for complex flows. Although it is very expensive, it is supposed to be superior in situations for which the anisotropy of turbulence has a dominant effect on the mean flow. This is especially true of highly swirling flows and stress-driven secondary flows.

With respect to computation, the one turbulence transport equation associated with the Spalart-Allmaras model is the least expensive turbulence model given the available options. The standard $\kappa-\varepsilon$ model and $\kappa-\omega$ model require more computational effort than the Spalart-Allmaras model since an additional transport equation is solved. Compared with the $\kappa-\varepsilon$ and $\kappa-\omega$ models, the RSM requires additional memory and CPU time due to the increased number of transport equations for Reynolds stresses. On average, the RSM requires 50-to-60% more CPU time per iteration and 15-to-20% more memory when compared to the $\kappa-\varepsilon$ and $\kappa-\omega$ models.

Table 1 CFD model specifications

Parameter	Definition	Value	Units
	Chamber Geometry		
L_c	Chamber length	2	in
D_c	Chamber diameter	2	in
L/D	Length-to-diameter ratio	1	
L_t	Throat length	0.1	in
D_t	Throat diameter	0.5	in
A_t	Throat area	0.196	in^2
CR	Contraction ratio	16	
L^*	Characteristic. length	32	in
D_e	Nozzle exit diameter	0.707	in
A_e	Nozzle exit area	0.393	in^2
A_e/A_t	Area ratio	2	-
	GOX Swirl Injector Species (swirl from aft-end)		
N_{inj}	Number of GOX injectors	4	-
D_{port}	Individual port diameter	0.111	in
A_{inj}	Total injection area	0.039	in^2
	GOX Secondary Injector Species (axial through faceplate)		
N_{inj}	Number of GOX injectors	1	-
D_{port}	Individual port diameter	0.111	in
A_{inj}	Total injection area	0.0097	in^2
	GH_2 Radial Injector Species (radial at head-end)		
N_{inj}	Number of GH2 injectors	4	-
D_{port}	Individual port diameter	0.102	in
A_{inj}	Total injection area	0.033	in^2

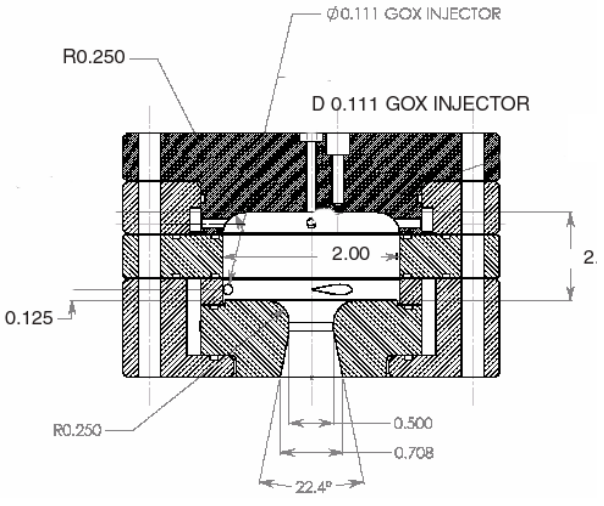

Fig. 1 Chamber geometry used in the CFD model.

For the cold flow study, we first run the simulation with the standard $\kappa - \varepsilon$ model; after convergence, we then activate the RSM model.

In the reactive flow model, the gaseous species are to be defined. The code we employ provides several models for modeling reacting flows. These include the generalized finite-rate model, the non-premixed combustion model, the premixed combustion model, and the partially premixed combustion model.

The generalized finite-rate model is based on the solution of transport equations for species mass fractions; to begin, one must define the chemical reaction mechanism for this model. The reaction rates are computed from Arrhenius rate expressions, from the eddy dissipation model of Magnussen and Hjertager,[11] or from the EDC model.

In the non-premixed combustion model individual species transport equations are not solved. Instead, transport equations for one or two conserved scalars (the mixture fractions) are solved and individual component concentrations are derived from the predicted mixture fraction distribution. In the conserved scalar approach, turbulence effects are accounted for with the help of a probability density function (PDF). Here we do not need to define the reaction mechanisms and, instead, the reacting system is treated using chemical equilibrium calculations. This we find to be the most convenient scheme.

The premixed combustion model is developed for combustion systems that are of the purely premixed type. In these problems perfectly mixed reactants and burned products are separated by a "flame front". The "reaction progress variable" is solved to predict the position of this front. The influence of turbulence is accounted for by means of a turbulent flame speed.

The partially premixed combustion model is used for systems that have a combination of non-premixed and perfectly premixed combustion. The mixture fraction equations and the reaction progress variable are solved to determine the species concentrations and position of the flame front, respectively.

In this study, we first use the generalized finite-rate model; this scheme is suitable for a wide range of applications including premixed, partially premixed, and non-premixed combustion. We then settle for the non-premixed combustion model with PDF.

When we first used the eddy dissipation model in conjunction with the one-step global combustion scheme, convergence was achieved with relative ease. However, the maximum temperature was over-predicted by approximately 1000 K.

After several trials, we have determined that the non-premixed combustion model is a suitable option for simulating the reactive flow. To use the non-premixed combustion model, it is necessary to calculate a non-adiabatic PDF table using prePDF™.[10] This information is then to be read from the PDF table into the code. To calculate the non-adiabatic flame temperature we need to first calculate the adiabatic flame temperature and use it as the maximum temperature in the non-adiabatic system calculation. The mean flame temperature estimate for non-adiabatic combustion is shown in Fig. 2. From this chart a non-adiabatic flame temperature of about 3800 K can be extrapolated. After selecting the non-premixed combustion model in the species panel, the PDF file containing the look-up tables can be read into the solver.

In controlling the solution, all the discretization schemes are set to first-order upwind. Once convergence is achieved by using these discretization schemes they are changed into second-order upwind schemes that are more accurate. After defining the boundary conditions and material properties, the code is then initialized and executed. The convergence criterion we have adopted is based on a tolerance that ensures

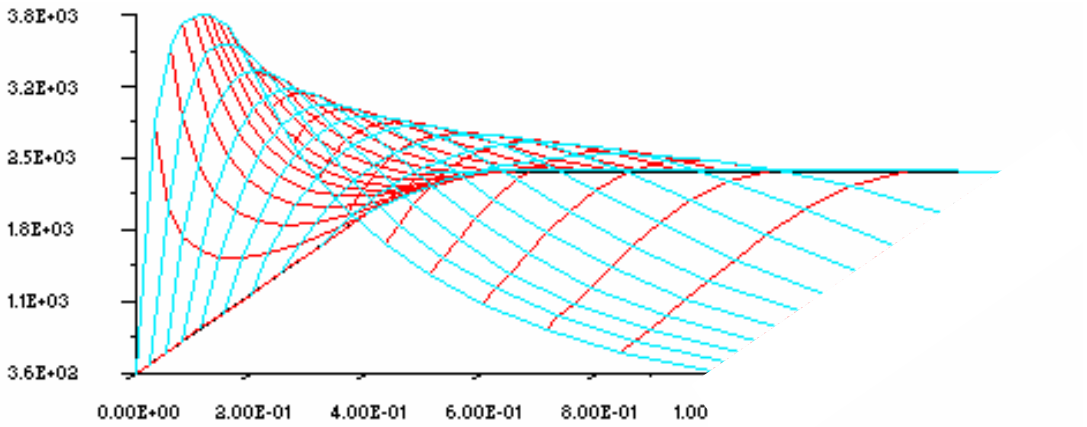

Fig. 2 Display of the mean flame temperature from the 3-D probability density function (PDF) table.

that the residual error remains less than 10^{-3} in the momentum balance, and less than 10^{-6} in the energy balance. To accelerate the convergence, we set the relaxation factors to be sufficiently small.

III. Results and Discussion

To simplify the calculations, here we do not include the nozzle effect, thus appending the nozzle outlet as a straight tube. Because the injection Mach number is 0.36, we can assume the flow to be nearly incompressible.

A. Cold Flow Simulation

To carry out the cold flow simulation that confirms the presence of a bidirectional flow, we use four oxygen inlet boundary conditions and one outlet boundary condition for the outflow at the base. Other boundary conditions include the default hard interior of the wall created by the mesh generator. The corresponding grid is shown in Fig. 3.

The non-reactive solution reaches convergence after approximately 400 iterations with the standard $\kappa - \varepsilon$ model; an additional 200 iterations are generally required to reach convergence with the RSM model. Typical flow pathlines that track the motion of an oxidizer particle are shown in Fig. 4. This plot clearly displays an outer vortex spiraling toward the head end and an inner vortex spiraling toward the nozzle. The flow reversal at the head end can be observed in Fig. 4b where the radius of the spiraling pathline gradually diminishes before reversing axial motion.

It should be noted that the pitch of the pathline shown in Fig. 4b changes across the chamber length. It is very small near the endwalls and largest halfway across the chamber. This result is gratifying because it confirms the increase in swirl intensity near the endwalls where fuel injection is achieved. From a practical standpoint, it justifies the placement of fuel injection near the head end where mixing due to swirl is maximized. In fact, this numerical finding lends support to the conclusion reached in the companion study by Vyas, Majdalani and Chiaverini[12] in which an analytical solution for the swirl intensity is derived; according to the theoretical model, the swirl intensity is expected to

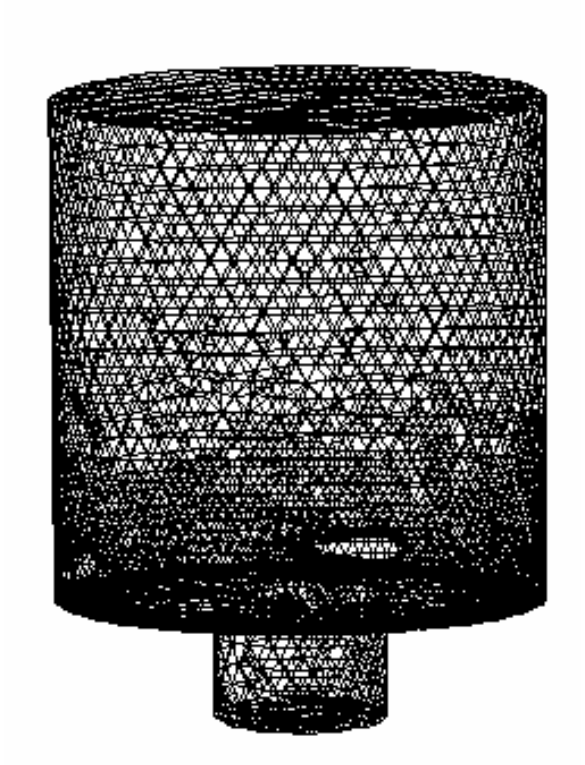

Fig. 3 Geometric grid.

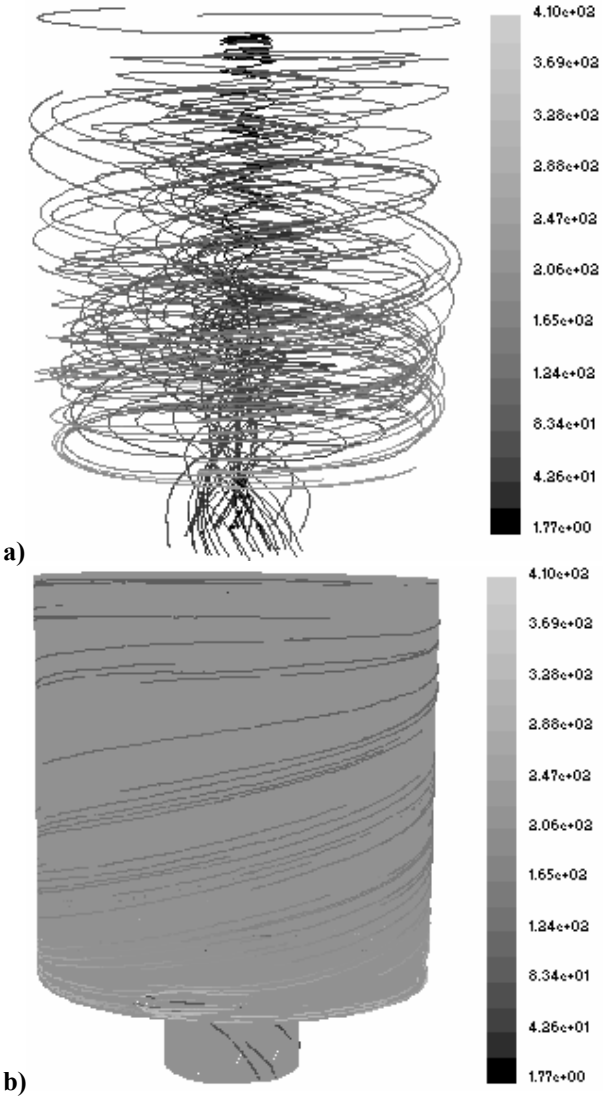

Fig. 4 Colored pathlines along a) the interior and b) the wall.

be the largest near the head end.

Details of the velocity character may be extrapolated from Fig. 5 where the axial, tangential, and radial velocity profiles are plotted at four equally spaced axial stations; specifically, profiles are located at ratios of $\frac{1}{4}, \frac{1}{2}, \frac{3}{4}$ and 1 of the chamber length measured, in the numerical model, from the base rather than the head end. At the head end, note that all three components of the velocity vanish, as they should, in fulfillment of the no slip and no flow penetration boundary conditions.

Figure 5a confirms that the axial velocity vanishes not only at the sidewall, but also at an internal node where the flow switches polarity. The location of this internal point coincides with the position of the so-called *mantle* separating the inner vortex from the outer vortex occupying the annular region in which the incoming fluid spirals toward the head end.[12-14] It may be instructive to note that the mantle location appears to be approximately 0.74 of the chamber radius at all axial positions. This result appears to be in fair agreement with the average value of 0.72 obtained experimentally by Smith[15] in his cylindrical gas cyclone with flat base. According to Smith, the mantle location also appeared to be weakly sensitive to the distance along the chamber length. This observation supports the theoretical estimate by Vyas, Majdalani and Chiaverini[12] who predicted a constant value of 0.707 from their inviscid solution of the bidirectional flow.

By analogy with unidirectional flow studies involving swirling motions, one may anticipate a forced vortex in the core region where viscous effects become appreciable. This is confirmed in Fig. 5b which displays features that one may attribute to a forced vortex in the core region and a free vortex in the outer region. Specifically, one may note the attenuation of the swirl velocity as one approaches the centerline. This result is in qualitative agreement with the explicit formulation obtained by Vyas, Majdalani and Chiaverini[13] where the forced vortex behavior is unraveled. It is also interesting to note that the tangential velocity profile does not change significantly as one crosses from $\frac{1}{4}$ to $\frac{3}{4}$ of the chamber length. This behavior also confirms the widely used assumption of an axially independent swirl velocity away from the endwalls. Such an assumption was actually necessary in deriving the analytical solution of the companion papers.[12-14]

Figure 5c shows the plot of the radial velocity component. Except for one case where the profile is artificially distorted due to turbulence and asymmetries in mesh discretization, the radial velocity is seen to follow the theoretical predictions associated with the analytical model.[12-14] Specifically, the profile is negative everywhere except along the sidewall and

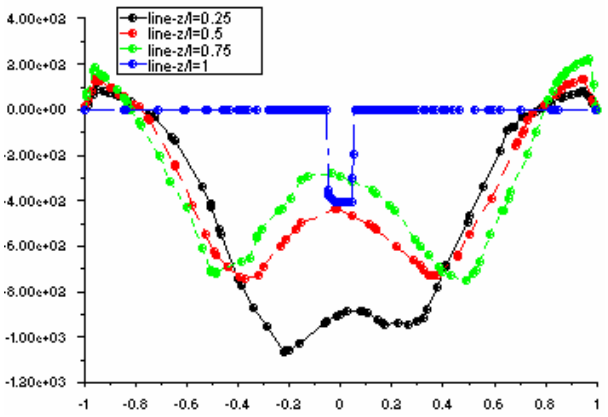

a) axial velocity

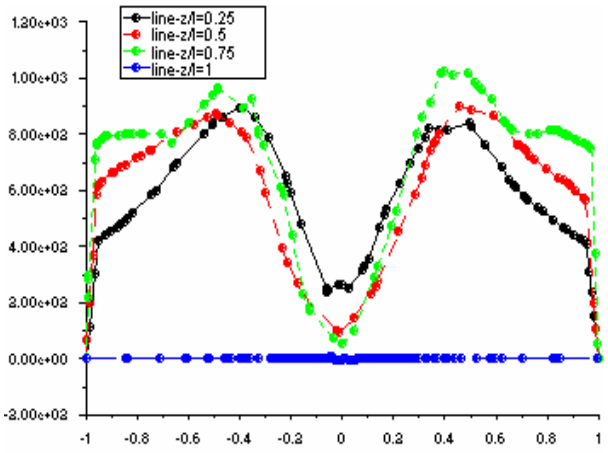

b) tangential velocity

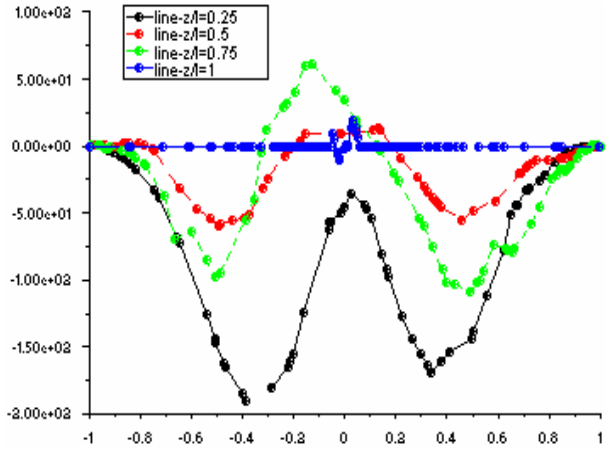

c) radial velocity

Fig. 5 Planar plot of a) axial, b) radial, and c) tangential velocity distributions along the chamber radius. All velocities are in ft/s.

along the centerline where forced vortex motion prevails. The negative radial velocity is appropriate of a flow that is always crossing from the outer, annular region to the inner vortex.

B. Reactive Flow Simulation

After simulating the cold flow, reactions are activated between oxygen and hydrogen (now injected at the top) to simulate the combustion environment in an actual CWBVCC vortex engine. In order to capture the proper species transport, the geometry is made to include four radial hydrogen inlets near the head end and a secondary axial oxygen inlet at the head end center to augment the flow issuing from the four tangential oxygen inlets near the base. To model the heat transfer across the outside wall, we define a cylindrical chamber of 0.1 in wall thickness. The geometry and associated mesh are shown in Fig. 6.

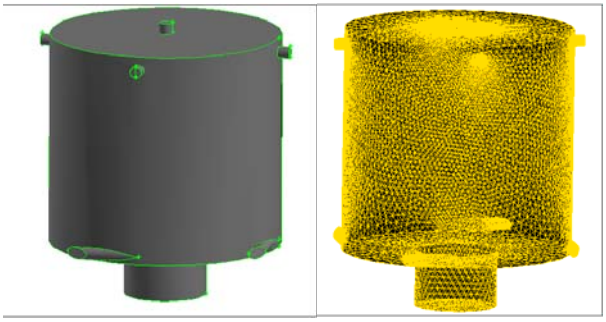

Fig. 6 Geometry and corresponding mesh layout.

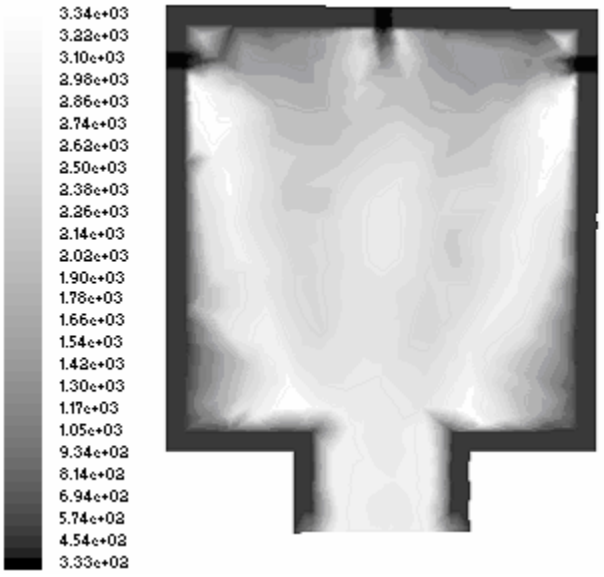

Fig. 7 Temperature contours in longitudinal plane.

After defining the boundary conditions and selecting the solver, the code is initialized and executed. To simulate the reactive flow, at first, the realizable $\kappa-\varepsilon$ model is employed; when the residual reaches a steady value, the scheme is changed to the RSM model (see Appendix A for further detail).

The static temperature contour is shown in Fig. 7. From Fig. 7, we can see that the highest flame temperature is approximately 3300 K; this result appears to be in good agreement with the value of 3294 K that is calculated at a pressure of 100 psia and a mixture ratio of 6 from the chemical equilibrium of

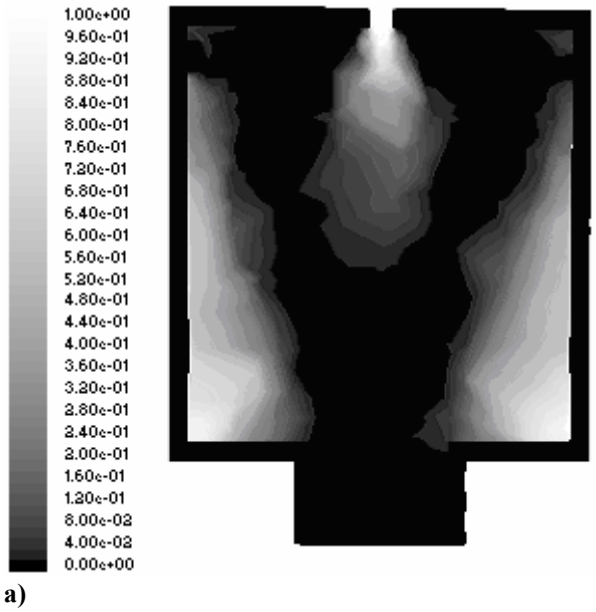

a)

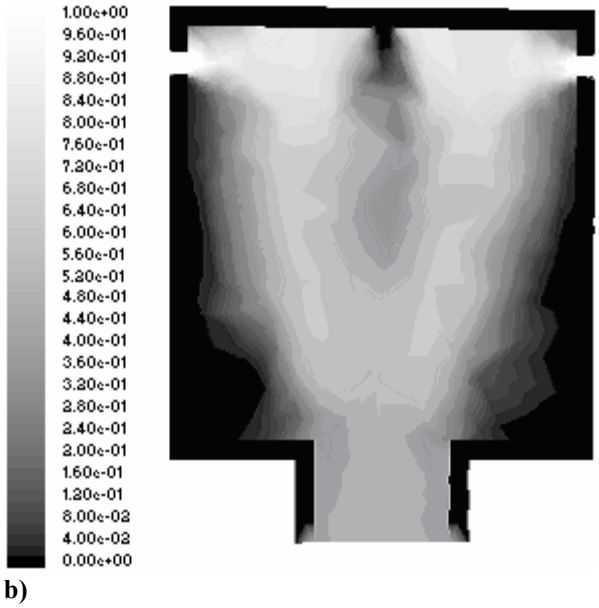

b)

Fig. 8 Species distribution for a) oxygen and b) hydrogen.

GOX/GH2 flames by Orbital Technologies Corporation (ORBITEC). The revolving W-shaped flame is caused by the secondary oxygen inlet from the top and the four radial inlets of hydrogen near the head end.

It should be noted that the higher temperatures are confined to the core region of the combustion chamber; conversely, the temperatures near the wall are fairly low. In fact, the average wall temperature is nearly 400 K. These estimates seem to concur with the experimental value of 383 K measured by ORBITEC for the same operating conditions. The lowered wall temperature is clearly caused by the cooling effect of the outer vortex which carries a chilled fluid.

As shown in Fig. 8a, the mass fraction of O_2 is largest near the wall. The attendant updraft protects the wall from overheating. Conversely, the mass fraction of H_2 shown in Fig. 8b is highest near the head end. This observation justifies ORBITEC's use of a secondary oxygen inlet at the center of the head end to protect the faceplate from thermal loading. As one may infer from the top section of Fig. 8b, the presence of secondary oxygen injection is rather mandatory to blow the hydrogen-rich reactants away from the head end wall. Conversely, one may infer from the lower section of Fig. 8b that traces of unburned hydrogen do accompany the flue gases. This observation is consistent with the use of a fuel rich combustion, especially when the equivalence ratio is 1.33 and the mixture ratio is 6.

The presence of unburned hydrogen can also be attributed to the high fuel and oxidizer speed at the injection ports (the inlet velocity of H_2 is about 477 m/s and that of O_2 is about 120 m/s). It is also due to the low temperature of the injectants (the injection temperatures of H_2 and O_2 are 366 K and 363 K, respectively).

Despite the impact of chemical reactions and their attendant heat release, a bi-directional field similar in essence to the cold flow described earlier is realized here. The corresponding mantle location, often used as a baseline in comparisons, is dislodged to approximately 0.75 of the chamber radius.

Based on Figs. 7 and 8, several practical modifications to the current engine design may be suggested. These include: a) injecting H_2 at a small angle below the horizontal (10-30 degrees); b) injecting O_2 at several spots that are equidistant from the center of the faceplate where secondary injection is currently present; and c) adding an upward pitch angle to oxygen injection at the base. These modifications may be attempted separately or in combination to produce an optimal configuration.

IV. Conclusions

In this study, a numerical simulation was presented as a tool for investigating the innovative cold-wall bidirectional vortex combustion chamber which seems to offer many technological advantages. The numerical simulations provided information for the bidirectional flowfield and verified the temperature maps inside the combustion chamber.

The simulations were first based on a two step process that required a convergent cold flow baseline prior to the activation of reactions. The viscous model we used in our cold flow simulation was the Reynolds Stress Transport Model (RSTM). According to Hoekstra, Derksen and Van den Akker,[4] RSTM is the only model to produce the trends observed in their experiments. In fact, RSTM is the only recommended model by the software developers for analyzing cyclonic flow. In the combustion simulation, a realizable $\kappa-\varepsilon$ model is used in conjunction with a non-premixed combustion scheme based on the PDF approach.

In the cold flow simulation, the peculiar features of the bidirectional flowfield were closely examined. The presence of high swirl intensity near the endwalls was also observed. The velocity profiles exhibited a non-translating layer at about 0.74 of the chamber radius.

The CFD results of the non-premixed combustion converged in predicting the cold-wall effect: The mass fraction of oxygen were found to be very high near the sidewall. The secondary oxygen injection was also found to be not only instrumental, but rather necessary to shield the faceplate.

Appendix A

At first, the eddy-dissipation model was used in conjunction with the one-step combustion model based on the global reaction $H_2 + \frac{1}{2}O_2 \rightarrow H_2O$. Here, H_2 and O_2 are assumed to undergo fast chemistry and complete combustion. In the process, all properties are expressed as function of temperature. The resulting flame temperature is over-predicted because the current scheme ignores numerous equilibrium equations.

The eddy-dissipation-concept (EDC) is an extension of the eddy-dissipation model that includes detailed chemical mechanisms in turbulent flow. It assumes that reactions occur in small turbulent structures, namely, the fine scales. Our next step was to use the EDC model to capture more realistically the combustion details. Here the classic 17 reaction steps are selected.[16] Using ' M' ' for H_2, 'f' for forward and 'b' for backward, these steps are enumerated below:

H_2/O_2 chain reactions:

1f) $O_2 + H \rightarrow OH + O$

1b) $OH + O \rightarrow O_2 + H$
2f) $H_2 + O \rightarrow OH + H$
2b) $OH + H \rightarrow H_2 + O$
3f) $H_2 + OH \rightarrow H_2O + H$
3b) $H_2O + H \rightarrow H_2 + OH$
4f) $OH + OH \rightarrow H_2O + O$
4b) $H_2O + O \rightarrow OH + OH$

HO_2 formation and consumption:
5f) $O_2 + H + M' \rightarrow HO_2 + M'$
5b) $HO_2 + M' \rightarrow O_2 + H + M'$
6) $HO_2 + H \rightarrow OH + OH$
7) $HO_2 + H \rightarrow H_2 + O_2$
8) $HO_2 + OH \rightarrow H_2O + O_2$
9) $HO_2 + H \rightarrow H_2O + O$
10) $HO_2 + O \rightarrow OH + O_2$

H_2O_2 formation and consumption:
11) $HO_2 + HO_2 \rightarrow H_2O_2 + O_2$
12f) $OH + OH + M' \rightarrow H_2O_2 + M'$
12b) $H_2O_2 + M' \rightarrow OH + OH + M'$
13) $H_2O_2 + H \rightarrow H_2O + OH$
14f) $H_2O_2 + OH \rightarrow H_2O + HO_2$
14b) $H_2O + HO_2 \rightarrow H_2O_2 + OH$

Recombination reactions:
15) $H + H + M' \rightarrow H_2 + M'$
16) $OH + H + M' \rightarrow H_2O + M'$
17) $O + O + M' \rightarrow O_2 + M'$

In the EDC model, detailed Arrhenius chemical kinetics are incorporated in turbulent flames; however, typical mechanisms are invariably stiff and their numerical integration is quite costly. The calculation is very expensive to the point of precluding a convergent solution. As a result, we have finally resorted to the non-premixed combustion model by using prePDF™ to prepare the lookup table and read it into the solver.

References

[1]ter Linden, A. J., "Investigations into Cyclone Dust Collectors," *Proceedings of the Institution of Mechanical Engineers,* Vol. 160, 1949, pp. 233-251.

[2]Bloor, M. I. G., and Ingham, D. B., "The Flow in Industrial Cyclones," *Journal of Fluid Mechanics,* Vol. 178, 1987, pp. 507-519.

[3]Hsieh, K. T., and Rajamani, R. K., "Mathematical Model of the Hydrocyclone Based on Physics of Fluid Flow," *AIChE Journal,* Vol. 37, No. 5, 1991, pp. 735-746.

[4]Hoekstra, A. J., Derksen, J. J., and Van den Akker, H. E. A., "An Experimental and Numerical Study of Turbulent Swirling Flow in Gas Cyclones," *Chemical Engineering Science,* Vol. 54, 1999, pp. 2055-2065.

[5]Dotson, K. W., Baker, R. L., and Bywater, R. J., "Systems Analysis of Launch Vehicle Aeroelastic Coupling," *4th International Symposium on Fluid Structure Interactions, Aeroelasticity, Flow Induced Vibration and Noise American Society of Mechanical Engineers, Aerospace Division*, 1997, pp. 53-3.

[6]Boysan, F., Ayers, W. H., and Swithenbank, J., "A Fundamental Mathematical Modelling Approach to Cyclone Design," *Institute of Chemical Engineers,* Vol. 60, 1982, p. 222.

[7]Zhou, L. X., and Soo, S. L., "Gas-Solids Flow and Collection of Solids in a Cyclone Separator," *Power Technology,* Vol. 63, 1990, p. 45.

[8]Dyakowski, T., and Williams, R. A., "Modelling Turbulent Flow within a Small-Diameter Hydrocyclone," *Chemical Engineering Science,* Vol. 48, 1993, p. 1143.

[9]Derksen, J. J., and Van den Akker, H. E. A., "Simulation of Vortex Core Precession in a Reverse-Flow Cyclone," *AIChE Journal,* Vol. 46, No. 7, 2000, pp. 1317-1331.

[10]*Fluent UNS Theory Manual*, 6.1 ed., Fluent Inc., Palo Alto, California, 2002.

[11]Magnussen, B. F., and Hjertager, B. H., "On Mathematical Models of Turbulent Combustion with Special Emphasis on Soot Formation and Combustion," International Symposium on Combustion The Combustion Institute Paper 16, 1976.

[12]Vyas, A. B., Majdalani, J., and Chiaverini, M. J., "The Bidirectional Vortex. Part 1: An Exact Inviscid Solution," AIAA Paper 2003-5052, July 2003.

[13]Vyas, A. B., Majdalani, J., and Chiaverini, M. J., "The Bidirectional Vortex. Part 2: Viscous Core Corrections," AIAA Paper 2003-5053, July 2003.

[14]Vyas, A. B., Majdalani, J., and Chiaverini, M. J., "The Bidirectional Vortex. Part 3: Multiple Solutions," AIAA Paper 2003-5054, July 2003.

[15]Smith, J. L., "An Analysis of the Vortex Flow in the Cyclone Separator," *Journal of Basic Engineering-Transactions of the ASME*, 1962, pp. 609-618.

[16]Peters, N., "Flame Calculations with Reduced Mechanisms: An Outline," *Reduced Kinetic Mechanisms for Applications in Combustion Systems*, edited by N. Peters and B. Rogg, Springer-Verlag, 1993.